



Cryo-EM Structure of an Atypical Proton-Coupled Peptide Transporter: Di- and Tripeptide Permease C

Maxime Killer^{1,2,3}, Giada Finocchio^{1,2}, Haydyn D. T. Mertens², Dmitri I. Svergun²,
Els Pardon^{4,5}, Jan Steyaert^{4,5} and Christian Löw^{1,2*}

¹Centre for Structural Systems Biology (CSSB), Hamburg, Germany, ²Molecular Biology Laboratory (EMBL), Hamburg Unit C/o Deutsches Elektronen Synchrotron (DESY), Hamburg, Germany, ³Collaboration for Joint PhD Degree Between EMBL and Heidelberg University, Faculty of Biosciences, Heidelberg, Germany, ⁴Structural Biology Brussels, Vrije Universiteit Brussel (VUB), Brussels, Belgium, ⁵VIB-VUB Center for Structural Biology, VIB, Brussels, Belgium

OPEN ACCESS

Edited by:

Arjen J. Jakobi,
Delft University of Technology,
Netherlands

Reviewed by:

Ekaitz Errasti Murugarren,
University of Barcelona, Spain
Giorgos Gouridis,
Foundation for Research and
Technology Hellas (FORTH), Greece

*Correspondence:

Christian Löw
christian.loew@embl-hamburg.de

Specialty section:

This article was submitted to
Structural Biology,
a section of the journal
Frontiers in Molecular Biosciences

Received: 11 April 2022

Accepted: 16 June 2022

Published: 11 July 2022

Citation:

Killer M, Finocchio G, Mertens HDT, Svergun DI, Pardon E, Steyaert J and Löw C (2022) Cryo-EM Structure of an Atypical Proton-Coupled Peptide Transporter: Di- and Tripeptide Permease C.
Front. Mol. Biosci. 9:917725.
doi: 10.3389/fmolb.2022.917725

Proton-coupled Oligopeptide Transporters (POTs) of the Major Facilitator Superfamily (MFS) mediate the uptake of short di- and tripeptides in all phyla of life. POTs are thought to constitute the most promiscuous class of MFS transporters, with the potential to transport more than 8400 unique substrates. Over the past two decades, transport assays and biophysical studies have shown that various orthologues and paralogues display differences in substrate selectivity. The *E. coli* genome codes for four different POTs, known as Di- and tripeptide permeases A-D (DtpA-D). DtpC was shown previously to favor positively charged peptides as substrates. In this study, we describe, how we determined the structure of the 53 kDa DtpC by cryogenic electron microscopy (cryo-EM), and provide structural insights into the ligand specificity of this atypical POT. We collected and analyzed data on the transporter fused to split superfolder GFP (split sfGFP), in complex with a 52 kDa Pro-macrobody and with a 13 kDa nanobody. The latter sample was more stable, rigid and a significant fraction dimeric, allowing us to reconstruct a 3D volume of DtpC at a resolution of 2.7 Å. This work provides a molecular explanation for the selectivity of DtpC, and highlights the value of small and rigid fiducial markers such as nanobodies for structure determination of low molecular weight integral membrane proteins lacking soluble domains.

Keywords: peptide transporter, SLC15, nanobody, Pro-macrobody, single particle cryo-EM, DtpC, YjdL, proton-dependent oligopeptide transporter

1 INTRODUCTION

Membranes of cells compartmentalize metabolic processes and present a selective barrier for permeation. To preserve the characteristic intracellular milieu, membrane transporters with specialized functions have evolved to maintain the nutrient homeostasis of cells (Hediger et al., 2013; Zhang et al., 2019). Many of those are energized by an electrochemical proton gradient, providing a powerful driving force for transport and accumulation of nutrients above extracellular concentrations. Proton-dependent oligopeptide transporters (POTs) of the Solute Carrier 15 family (SLC15) are representatives of such secondary active transport systems and occur in all living organisms except in Archaea. They allow an efficient uptake of peptides and amino acids in bulk quantities (Daniel et al., 2006; Thwaites and Anderson, 2007). The best characterized members are the two mammalian PepT1 and PepT2 transporters which are known to play crucial roles in human

health, being responsible for the uptake and distribution of nutrients such as di- and tripeptides (Brandsch et al., 2004; Smith et al., 2013; Spanier and Rohm, 2018; Viennois et al., 2018). They also play key roles in human diseases, and impact the pharmacokinetic profiles of orally administered drug molecules (Daniel, 2004; Brandsch, 2009; Ingersoll et al., 2012; Hillgren et al., 2013; Colas et al., 2017; Heinz et al., 2020). SLC15 transporters belong to the Major Facilitator superfamily (MFS). MFS transporters share a well-characterized fold, consisting of twelve transmembrane helices organized in two six-helix bundles, expected to function according to the alternate access mechanisms (Jardetzky, 1966) where either side of the transporter is alternately exposed to one side of the membrane. Therefore, substantial conformational changes are required to complete an entire transport cycle with at least three postulated states: (i) inward-open, (ii) occluded, and (iii) outward-open (Yan, 2015; Drew and Boudker, 2016; Quistgaard et al., 2016; Bartels et al., 2021; Drew et al., 2021). POTs have been intensively studied on a structural and biochemical level over the last 30 years. More than 50 entries for this transporter class can be found in the protein data bank, representing ten different bacterial homologues and the mammalian PepT1 and PepT2 transporters, bound to a limited set of substrates and drugs (Newstead et al., 2011; Solcan et al., 2012; Doki et al., 2013; Guettou et al., 2013; Guettou et al., 2014; Lyons et al., 2014; Zhao et al., 2014; Quistgaard et al., 2017; Martinez Molledo et al., 2018a; Martinez Molledo et al., 2018b; Minhas et al., 2018; Nagamura et al., 2019; Ural-Blimke et al., 2019; Killer et al., 2021; Parker et al., 2021; Shen et al., 2022; Stauffer et al., 2022). Although bacterial and eukaryotic POTs share an overall conserved binding site, individual amino acids changes in or in close vicinity of the binding site are likely responsible for observed differences in affinities and selectivity for particular peptides and drugs among the studied POT homologues. Here, structural biology studies are particularly crucial to understand substrate promiscuity and drug coordination on a molecular level. While bacterial POT structures, determined by mainly X-ray crystallography, represent exclusively the inward-open or inward-open-partially occluded state, the mammalian PepT1 and PepT2 transporters were recently captured in various conformations by single particle cryo-EM, advancing the mechanistic understanding of the entire transport cycle (Killer et al., 2021; Parker et al., 2021). Despite their small size of typically only 50 kDa for an individual transporter unit, these systems become more and more accessible for single-particle cryo-EM approaches. Indeed, in 2021, more MFS transporter structures were determined by single-particle Cryo-EM (17 pdb entries; resolution range 3.0–4.2 Å) than X-ray crystallography (14 pdb entries; resolution range 1.8–3.6 Å).

Although known POT structures show a high level of similarity, various works have indicated that homologues can differ in their range of transported substrate and drug molecules (Lyons et al., 2014; Prabhala et al., 2014; Boggavarapu et al., 2015; Sharma et al., 2016; Martinez Molledo et al., 2018a). The *E. coli* genome codes for four different POTs named Di- and tripeptide permease A-D (DtpA-D), also known as YdgR (=DtpA), YhiP (=DtpB), YjdL (=DtpC) and YbgH (=DtpD). They cluster in

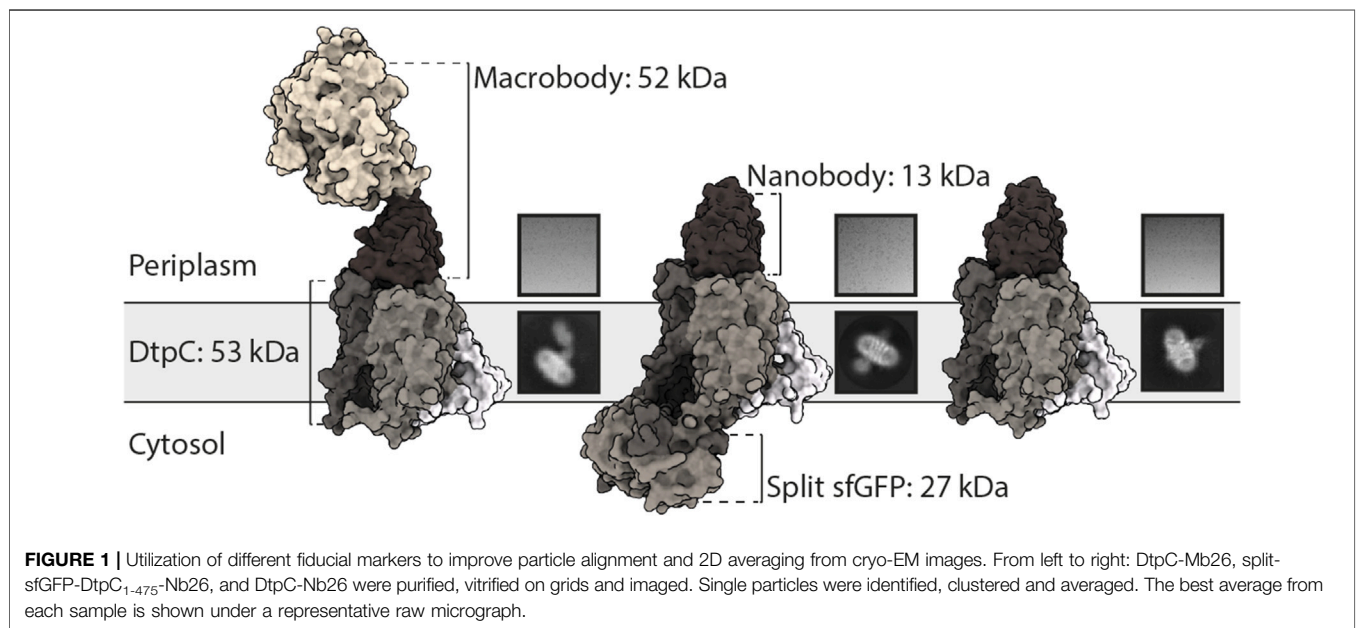
pairs, DtpA and B (sequence identity 51%), and DtpC and D (sequence identity 56%) with around 25% identity between them. DtpA and B exhibit a prototypical substrate preference similar to the human PepT1 transporter (Chen et al., 2000; Harder et al., 2008; Foley et al., 2010; Prabhala et al., 2017; Prabhala et al., 2018), while DtpC and D have been classified as atypical POTs, because DtpC prefers dipeptides in particular those with a lysine residue in the second position. Although DtpC has been well characterized in terms of function over the last years (Ernst et al., 2009; Jensen et al., 2012a; Jensen et al., 2012b; Jensen et al., 2012c; Jensen et al., 2014; Prabhala et al., 2014; Aduri et al., 2015), it has resisted structure determination by X-ray crystallography so far (Gabrielsen et al., 2011).

Here we describe the structure determination of the bacterial POT transporter DtpC by single particle cryo-EM. Considering that the transporter displays no characteristic cytoplasmic or periplasmic features which are helpful to drive the particle alignment, we applied different strategies previously described in the literature to increase the overall size of the transporter to overcome these limitations. We i) fused the transporter to split-sfGFP (Liu et al., 2020; Liu et al., 2022), ii) raised different nanobodies against DtpC (Pardon et al., 2014) and iii) extended the nanobody to a Pro-macrobody (Brunner et al., 2020; Botte et al., 2022). The various samples were subsequently imaged by cryo-EM and analysed. DtpC in complex with the conformation specific nanobody 26 turned out to be more rigid and a significant fraction of the sample dimeric, allowing us to reconstruct DtpC to 2.7 Å resolution. The DtpC structure now provides molecular insights into how selectivity within this transporter family is achieved.

2 RESULTS AND DISCUSSION

2.1 Different Fiducial Marker Strategies for Structure Determination

Since MFS transporters typically lack additional domains outside their transport unit, which is a major impediment for accurate particle alignment in single particle cryo-EM approaches, we assessed three fiducial marker strategies introducing additional density outside of detergent micelles containing DtpC, by analyzing the quality of 2D class averages (**Figure 1**). To obtain conformation specific binders against DtpC, we first immunized llamas with recombinant DtpC and selected nanobodies (Nbs) following standard procedures (Pardon et al., 2014). Three out of five selected binders (Nb17, Nb26, and Nb38) co-eluted with DtpC on gel filtration (**Supplementary Figure S1**) and increased the melting temperature of the respective DtpC-Nb complex by 20°C, 16°C, and 12°C. (**Figures 2A,B**). DtpC in complex with Nb17 and Nb26 yielded crystals in various conditions, but despite extensive optimization efforts, the crystals of the DtpC-Nb26 complex did not diffract X-rays better than 5 Å resolution. In a second step, we decided to increase the size of Nb26, which formed a tight complex with DtpC, by fusing one copy of the maltose binding protein (MBP) to its C-terminus as described previously (Botte et al., 2022). This resulted in a



52 kDa Pro-macrobody (short Mb26), and we expected it to bind to the periplasmic side of the transporter as seen in other MFS transporter-Nb complexes (**Figure 1**). In a third approach, we fused the two self-assembling parts of split-sfGFP; with β 1-6 on the N-terminus of DtpC, and β 7-11 on the C-terminus. We named this construct split sfGFP-DtpC_{FL}. In order to minimize the mobility between the membrane protein and the split sfGFP fiducial, we also generated two additional constructs where the last five (split sfGFP-DtpC₁₋₄₇₅), or ten residues (split sfGFP-DtpC₁₋₄₇₀) of the transporter were deleted. We then assessed proper folding and complementation by monitoring the fluorescence of the chromophore on an HPLC system (**Figure 2C**). All constructs eluted at similar retention times and the fluorescence was highest in the non-truncated construct (split sfGFP-DtpC_{FL}) and lowest in the most truncated version (split sfGFP-DtpC₁₋₄₇₀). In order to extend this observation to other MFS transporters, we repeated this experiment with the human POT homologue PepT1, and noticed a similar trend upon shortening of the termini. Yet, since the decrease of fluorescence was only minor in split sfGFP-DtpC₁₋₄₇₅ in comparison to split sfGFP-DtpC_{FL}, we proceeded to imaging with the shorter construct in the presence of Nb26.

The particle density and distribution in the vitrified solution was similar in the three imaged samples. However, DtpC-Nb26 produced the best 2D class averages considering the sharpness of secondary structure elements inside the micelle, as judged by visual inspection (**Figure 1**, **Supplementary Figure S2**). The Pro-macrobody Mb26 fiducial was clearly visible in 2D class averages, but it adopted various positions in relation to the transporter, therefore making accurate alignment of the particles more difficult than in its shorter but more rigid and stable nanobody version (**Figure 1**, **Figure 3A, B**, **Supplementary Figure S2**). The split sfGFP-DtpC₍₁₋₄₇₅₎-Nb26 sample allowed

clear visualization of the transmembrane helices after clustering a small subset of particles, but the majority of particles clustered in classes with blurry density for the split sfGFP fiducial, or with the two complementary parts β 1-6 and β 7-11 not assembled (**Supplementary Figure S2**). AlphaFold2 predictions on the imaged construct, as well as on the full length construct later suggested a destabilization of the beta-barrel upon increasing termini restrains, resulting in partial unfolding of β 7 and exposure of the chromophore to solvent quenching. Interestingly, this effect could partially be reverted by adding a linker of five glycine residues between the C-bundle and β 7 based on *in silico* data. We conclude that termini restraining using the split-sfGFP approach is a promising fiducial strategy for structural studies of MFS transporters, in addition to the previous demonstrated showcases on small membrane proteins (2, 4 and 6TMs) (Liu et al., 2020; Liu et al., 2022). However, the amount of restraining in larger membrane proteins such as MFS transporters where both termini are placed far from each other need to be optimized experimentally or *in silico*, to produce a stable and rigid fiducial; two crucial aspects for high resolution structure determination of MFS transporters by single particle cryo-EM.

As we obtained the best 2D class averages for DtpC with the fiducial marker Nb26, we proceeded to a large data collection (**Table 1**) and could cluster a subset of dimers within this data set (**Figure 3**). The presence of different oligomeric species was already expected based on the peak shape of the gel filtration run (**Figure 4A**). The large mass of the dimer, and the stable and rigid signal of the Nb26 fiducial, allowed us to reconstruct the DtpC-Nb26 dimer to 3.0 Å resolution and model this assembly (**Figures 3, 4**, **Supplementary Figure S3**). The quaternary structure consists of a non-symmetrical inverted dimer mediated by interactions through a large hydrophobic interface between the HA-HB helices of DtpC (**Supplementary Figure S3**). Although other inverted dimers were reported in

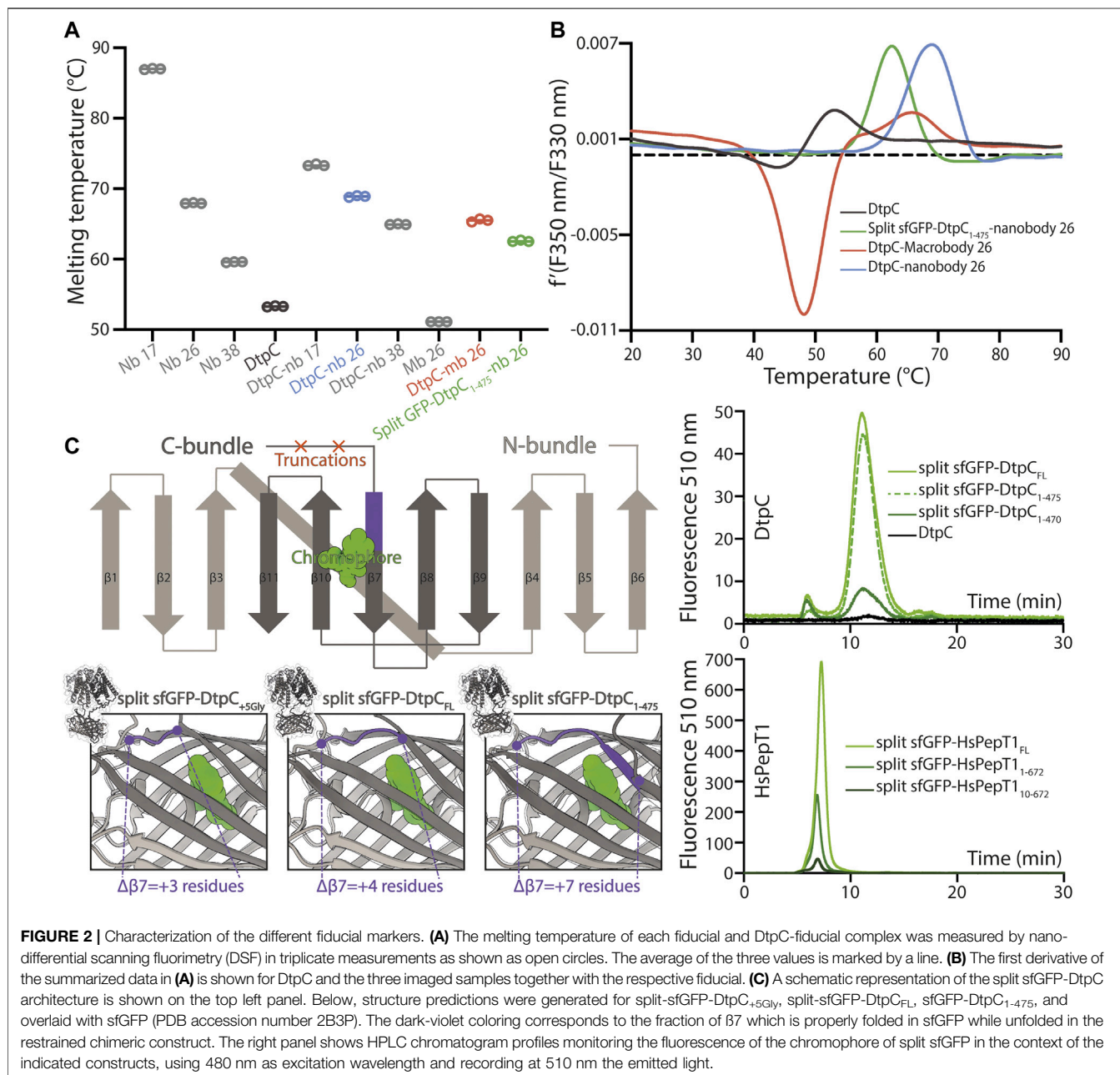


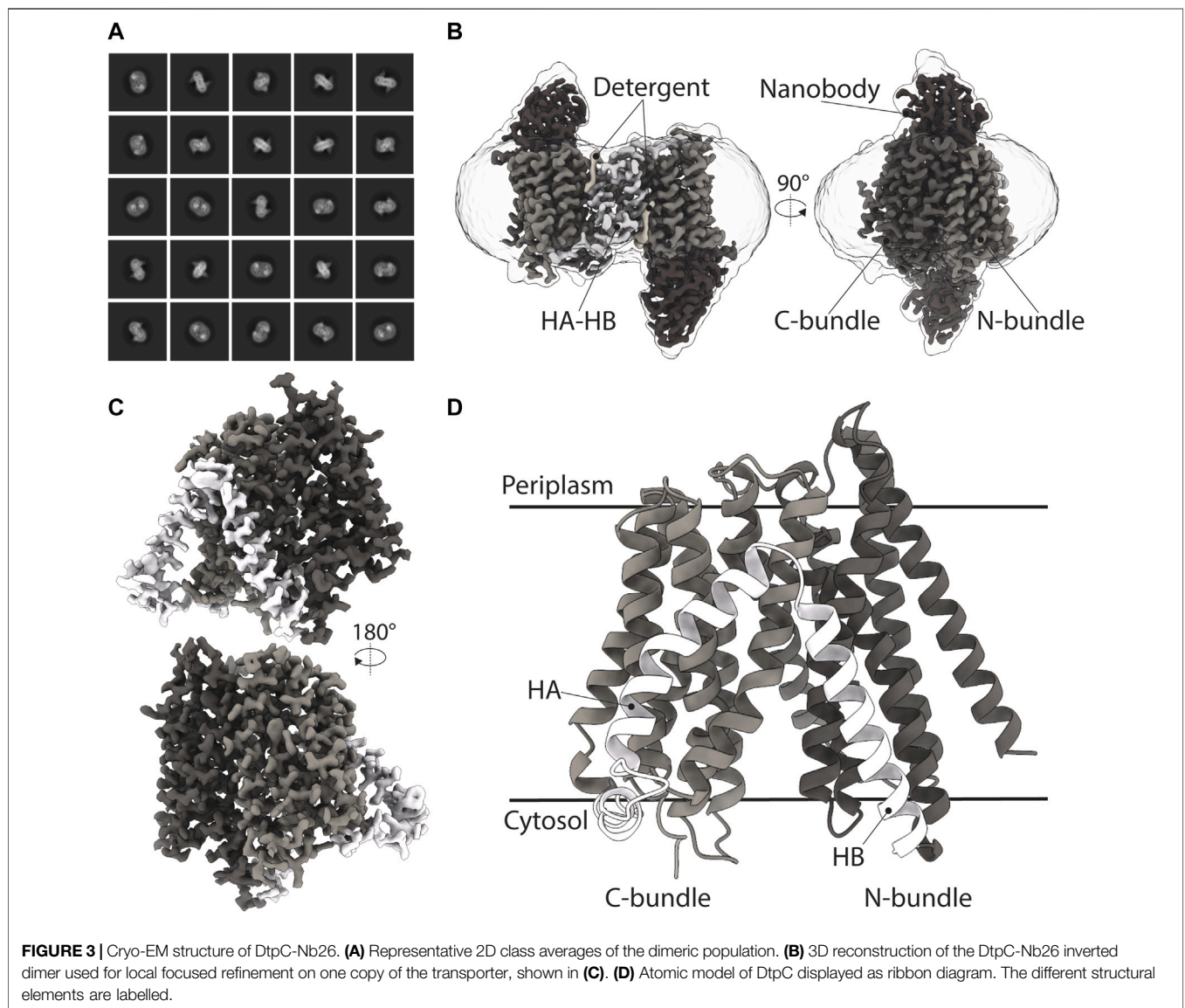
FIGURE 2 | Characterization of the different fiducial markers. **(A)** The melting temperature of each fiducial and DtpC-fiducial complex was measured by nano-differential scanning fluorimetry (DSF) in triplicate measurements as shown as open circles. The average of the three values is marked by a line. **(B)** The first derivative of the summarized data in **(A)** is shown for DtpC and the three imaged samples together with the respective fiducial. **(C)** A schematic representation of the split sfGFP-DtpC architecture is shown on the top left panel. Below, structure predictions were generated for split-sfGFP-DtpC_{+5Gly}, split-sfGFP-DtpC_{FL}, split-sfGFP-DtpC₁₋₄₇₅, and overlaid with sfGFP (PDB accession number 2B3P). The dark-violet coloring corresponds to the fraction of β7 which is properly folded in sfGFP while unfolded in the restrained chimeric construct. The right panel shows HPLC chromatogram profiles monitoring the fluorescence of the chromophore of split sfGFP in the context of the indicated constructs, using 480 nm as excitation wavelength and recording at 510 nm the emitted light.

homologous POT structures (Quistgaard et al., 2017), the source of such arrangements is likely to be artificial. We also investigated the oligomer heterogeneity in solution with small angle X-ray scattering and obtained a good fit at low angles (corresponding to the overall shape of particles in solution) for the cryo-EM volume of the dimer (**Supplementary Figure S4**). The fit to a monomeric cryo-EM volume was poor, indicating that in detergent solution a significant fraction of DtpC-Nb26 is dimeric. As for the interaction between the membrane protein and the fiducial marker, the CDR3 loop of Nb26 accounts for the strongest interactions with the periplasmic surface of the transporter with two salt bridges, while CDR1 and CDR2 contribute via

hydrogen bonding (**Figure 5**). 3D variability analysis (Punjani and Fleet, 2021) revealed a small degree of flexibility between the two DtpC-Nb26 copies. Therefore, we performed a local refinement, focused on one copy of the membrane protein, which extended the resolution of the reconstruction to 2.7 Å and improved the accuracy of the atomic model for subsequent structural analysis (**Figure 4**).

2.3 Structural Basis for Ligand Selectivity in DtpC

The DtpC structure revealed the expected and well-known MFS transporter fold, with twelve transmembrane helices (TMs)



organized in two helical bundles and additional two TMs specific for the POT family (known as HA and HB domains). It is highly similar compared to the previously determined DtpD structure (Zhao et al., 2014) with an overall RMSD value of 1.06 Å between the two (for 335 out of 436 C_α-atoms). The peptide binding site of DtpC is exposed to the cytoplasmic side (Figures 3, 4). Almost all bacterial POT structures described so far were determined by X-ray methods in a similar inward facing (IF) conformation. The extent to which the central cavity is open to the cytosol is regulated by a mechanism of occlusion mediated by TM4, TM5, TM10, and TM11, as supported by structures in IF occluded, partially occluded, and open states. In the case of the here described DtpC structure, the IF state is open (Figure 3).

Molecules from the periplasmic side, on the contrary, cannot enter the central cavity. Tight closure of both bundles above the binding site is mediated by a salt bridge between D43 (TM2, N-bundle) and R294 (TM7, C-bundle) and hydrogen bonds

between H37 (TM1, N-bundle) and D293 (TM7) as well as R28 (TM1) and N421 (TM11, C-bundle) (Figure 6A). We also analyzed previously determined POT structures with clearly resolved side chain densities, to understand how the IF state is generally maintained in this transporter family. Except for human PepT2 and the POT transporter from *Shewanella oneidensis* (PepT_{So}), where the inter-bundle periplasmic salt bridge is formed between TM5 and TM7, the IF state is in all other analyzed structures stabilized by a salt bridge on the tip of TM2 and TM7 (Figure 6B). Additional hydrogen bonding networks as described in other studies, can occur, but vary greatly among different homologues. This analysis highlights that the alternate access mechanism in canonical and in so called 'atypical' POTs share similarities such as electrostatic clamping by formation and disruption of salt bridges. The differences in hydrogen bonding patterns however, could account for the various turnover rates seen among POT homologues.

TABLE 1 | Data collection and refinement statistics of the deposited DtpC structure.

Protein Reconstructed	Di- and Tripeptide Permease C (DtpC)
PDB accession code	7ZC2
EMDB accession code	EMD-14618
Data acquisition	
Microscope/Detector	Titan Krios/Gatan K3
Imaging software	EPU
Magnification	105,000
Voltage (kV)	300
Electron exposure (e-/Å ²)	75
Dose rate (e-/pix/s)	19.5
Frame exposure (e-/Å ²)	1.5
Defocus range (µm)	-0.9 to -1.8
Physical pixel size (Å)	0.85
Micrographs	24,333
Reconstruction	
Picked coordinates (cryolo)	6,464,070
Particles in 3D classification (RELION)	6,365,235
Particles in final refinement (CryoSPARC)	878,428
Symmetry imposed	C1
Map sharpening method	Phenix Resolve_cryo_em
Map resolution, FSC _{half maps; 0.143 masked/unmasked} (Å)	2.72/3.43
Refinement	
Initial model used for refinement	AlphaFold2 model, relaxed with Amber
Model resolution (Å)	
FSC 0.143, masked/unmasked	2.64/5.43
Model composition	
Non-hydrogen atoms	7334
Protein residues	471
ADP B factor (Å ²) mean	12.73
R.m.s deviations	
Bond lengths (Å) (#>4σ)	0.003 (0)
Bond angles (°) (#>4σ)	0.616 (0)
Validation	
MolProbity score	1.44
Clashscore	8.04
Rotamer outliers (%)	0.00
Ramachandran plot	
Favored (%)	98.29
Allowed (%)	1.71
Outliers (%)	0.00

Canonical POTs are characterized by i) the presence of the E₁XXE₂R motif on TM1 involved in proton coupling and ligand binding, and ii) the ability to accommodate dipeptides, tripeptides, and peptidomimetics, which relies on a set of conserved residues located in the central binding cavity. In DtpC, the E₁XXE₂R motif, has evolved to Q₁XXE₂Y (where Q₁ = N17, E₂ = E20, Y=Y21). In all high resolution X-ray structures of canonical POTs, R is in salt-bridge distance to E₂ and the C-terminus of substrate peptides. Mutation of either E₁ or E₂ in the conventional E₁XXE₂R motif to glutamine residues abolishes uptake (Aduri et al., 2015). A reverse mutation in DtpC, from Q₁XXE₂Y to E₁XXE₂Y or to E₁XXQ₂Y preserves high transport rates, while a Q₁XXQ₂Y motif significantly decreases it (Aduri et al., 2015). In addition, based on previous molecular dynamics experiments, a salt bridge switching mechanism from R-E₂ to R-E₁, upon protonation of E₂ in the E₁XXE₂R motif, was proposed (Aduri et al., 2015). This biochemical and *in silico*

data strongly support a dual role of the E₁XXE₂R motif for both proton and peptide transport, where R can form a salt bridge interaction with the C-terminus of peptides or with E₁ when E₂ is protonated, and where the deprotonation event of the latter is required to disrupt the R-peptide interaction.

In DtpC, we now observe that the side chain pocket has a different architecture and characteristic in comparison with the one of canonical POTs. It displays an overall more acidic groove caused by the presence of the aspartate residue 392, conserved among atypical POTs. This residue has been predicted to be involved in substrate coordination and mutation of this residues in DtpC and homologues DtpD (corresponding residue is D395) abolished transport activity (Jensen et al., 2012b; Zhao et al., 2014). Canonical POTs have a conserved serine residue instead, yielding a slightly changed hydrophobicity pattern in the binding site (Figures 7A–D). A structural overlay of DtpC with a canonical POT structure bound to the dipeptide Ala-Phe allows us to position the peptide in the binding site. By replacing the phenyl group with a lysine side chain (generating the known DtpC dipeptide substrate Ala-Lys instead of Ala-Phe), we postulate a putative salt bridge between the carboxyl group of D392 and the ε-amino group of the lysine side chain. This observation, together with previous biochemical work (Jensen et al., 2012b; Aduri et al., 2015) allows us to hypothesize that the selectivity of DtpC for dipeptides with C-terminal lysine or arginine residues is caused by swapping a salt bridge between the recurrent carboxyl group of the peptide terminus and the transporter (R21Y mutation), to a side chain specific salt bridge with D392. Since the R-peptide interaction is lost in DtpC, there is no requirement for E1 to destabilize R-peptide for release, which would explain the presence of a Q₁XXE₂Y motif instead of E₁XXE₂R.

In summary, our work provides new insights into promiscuous versus selective substrate recognition in POTs and constitutes a step forward towards completing the family of *E. coli* POTs structures. Lastly, it displays some of the challenges related to high resolution cryo-EM structure determination of MFS transporters devoid of soluble domains, and manifests once again, the benefit of fiducial markers in overcoming those.

3 MATERIAL AND METHODS

3.1 Expression and purification of membrane protein constructs: DtpC; split sfGFP-DtpC (full length split sfGFP-DtpC_{FL}, and truncated constructs split sfGFP-DtpC₁₋₄₇₅ and split sfGFP-DtpC₁₋₄₇₀); split sfGFP-HsPepT1 (full length split sfGFP-HsPepT1_{FL}, and truncated constructs split sfGFP-HsPepT1₁₋₆₇₂ and split sfGFP-HsPepT1₁₀₋₆₇₂)

The full-length cDNA of DtpC wild type (WT) was amplified from the *Escherichia coli* genome, and cloned into a pNIC-CTHF vector by ligation-independent cloning (LIC). This vector contains a

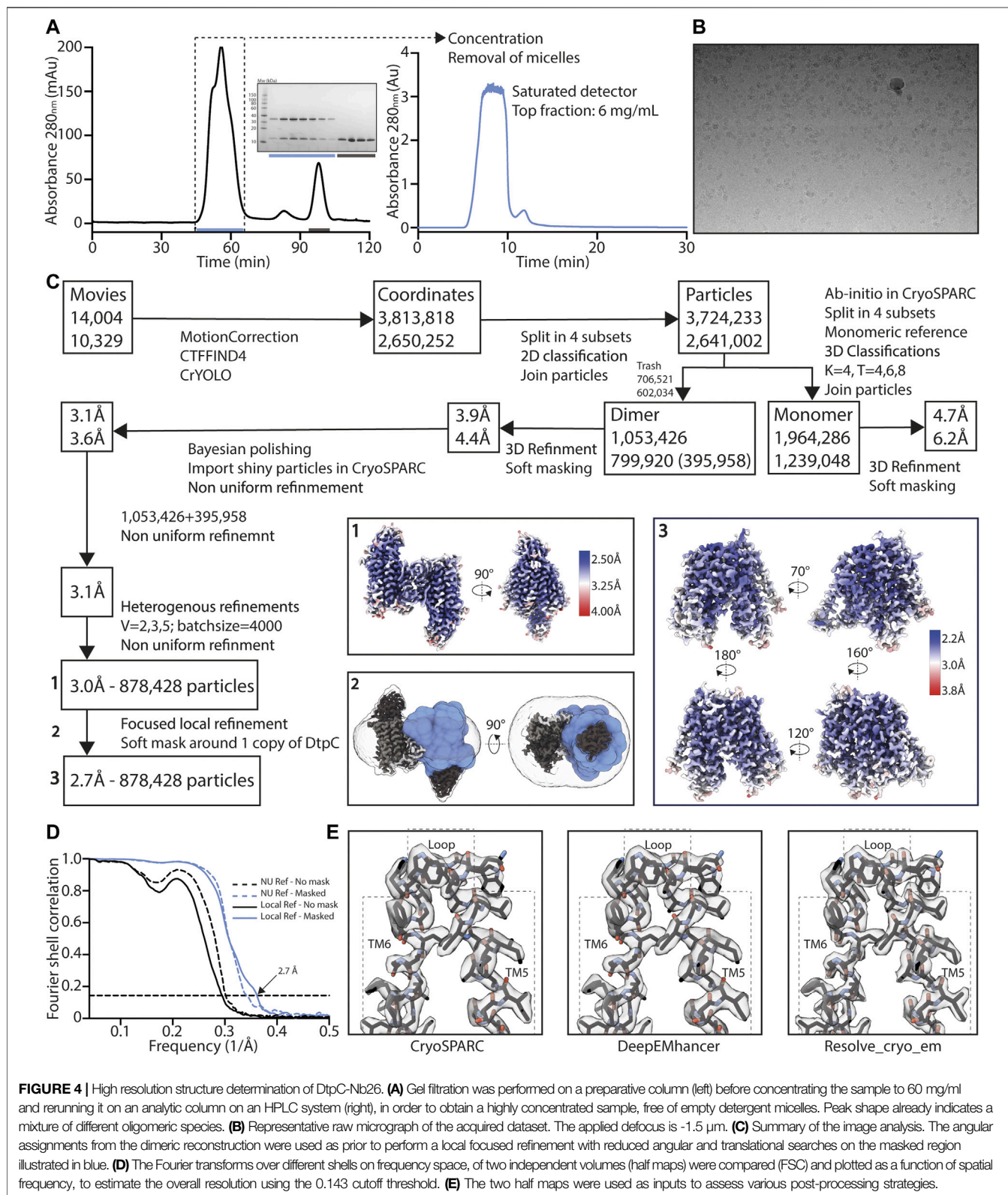
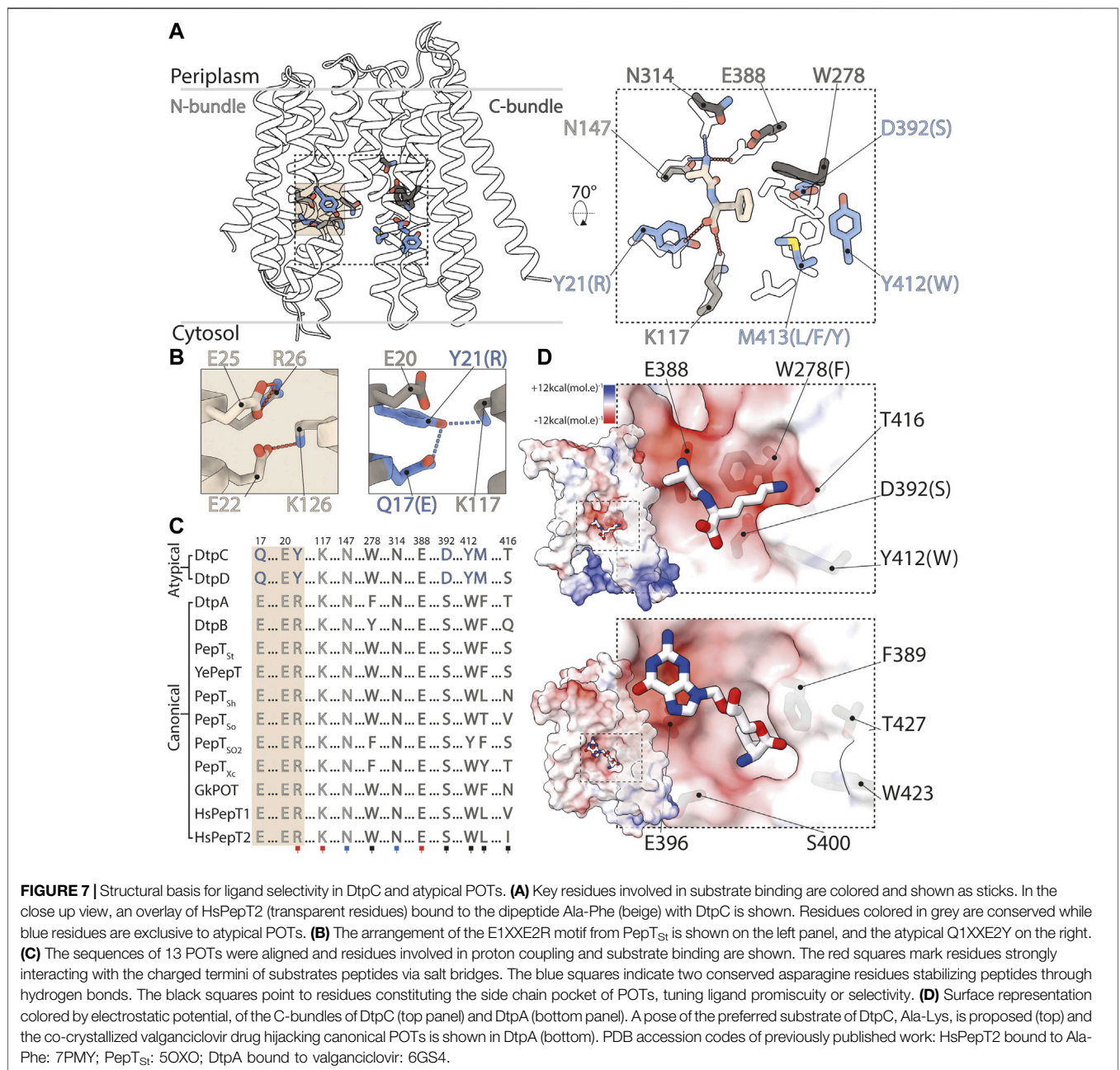


FIGURE 4 | High resolution structure determination of DtpC-Nb26. **(A)** Gel filtration was performed on a preparative column (left) before concentrating the sample to 60 mg/ml and rerunning it on an analytic column on an HPLC system (right), in order to obtain a highly concentrated sample, free of empty detergent micelles. Peak shape already indicates a mixture of different oligomeric species. **(B)** Representative raw micrograph of the acquired dataset. The applied defocus is $-1.5 \mu\text{m}$. **(C)** Summary of the image analysis. The angular assignments from the dimeric reconstruction were used as prior to perform a local focused refinement with reduced angular and translational searches on the masked region illustrated in blue. **(D)** The Fourier transforms over different shells on frequency space, of two independent volumes (half maps) were compared (FSC) and plotted as a function of spatial frequency, to estimate the overall resolution using the 0.143 cutoff threshold. **(E)** The two half maps were used as inputs to assess various post-processing strategies.

C-terminal His-Tag and a Tobacco Etch virus (TEV) cleavage site and a kanamycin resistance gene as selectable marker. The first 6 N-terminal beta strands of sfGFP were fused to the N-terminus of

DtpC, and the beta strands 7 to 11 fused to the C-terminus. We named this construct split sfGFP-DtpC_{FL}. Two additional constructs were cloned with truncations of 5 (split sfGFP-



DtpC₁₋₄₇₅), and 10 residues (split sfGFP-DtpC₁₋₄₇₀), on the C-terminal side of DtpC.

HsPepT1 was previously cloned into a pXLG vector containing an expression cassette composed of an N-terminal Twin-Streptavidin tag followed by the HRV-3C protease recognition sequence (Killer et al., 2021). Similarly, as for DtpC, the two self-assembling parts of split-sfGFP were first inserted into the N- and C-termini of the full-length version of HsPepT1, and on two other versions with i) a C-terminal truncation of 36 residues (split sfGFP-HsPepT11-672), and ii) a C-terminal truncation of 36 residues and a N-terminal truncation of 10 residues (split sfGFP-HsPepT110-672) were cloned.

Recombinant DtpC, and the three split sfGFP-DtpC constructs were expressed in *E. coli* C41(DE3) cells grown in

terrific broth (TB) media supplemented with 30 µg/ml kanamycin according to established procedures (Löw et al., 2012; Löw et al., 2013). Cultures were grown at 37°C and protein expression was induced with 0.2 mM IPTG at an OD_{600 nm} of 0.6–0.8. After induction, culture growth continued at 18°C for 16–18 h. Cells were harvested by centrifugation (10,000 × g, 15 min, 4°C), and the pellet was stored at -20°C until further use. Cell pellets were resuspended in lysis buffer (20 mM NaPi at pH 7.5, 300 mM NaCl, 5% (v/v) glycerol, 15 mM imidazole, with 3 ml of lysis buffer per Gram of wet weight pellet), supplemented with lysozyme, DNase and 0.5 mM tris(2-carboxyethyl)phosphine (TCEP). The cells were lysed by three cycles using an Avestin Emulsiflex homogenizer at 10,000–15,000 psi. Recovered material

was centrifuged to remove non-lysed cells ($10,000 \times g$, 15 min, 4°C) and the supernatant was subjected to ultracentrifugation to separate the membrane fraction ($100,000 \times g$, 1 h, 4°C using an Optima XE-90, Beckman Coulter centrifuge). Membranes were resuspended in lysis buffer supplemented with cOmplete EDTA-free protease inhibitors (Roche), and solubilized by adding 1% n-Dodecyl- β -D-Maltoside (DDM) detergent (Anatrace). The sample was centrifuged for 50 min at $90,000 \times g$, and the supernatant was applied to Ni-NTA beads for immobilized-metal affinity chromatography (IMAC) on a gravity column. The beads were pre-equilibrated in lysis buffer and incubated with the solubilized membrane proteins for one hour at 4°C on a rotating wheel. Loaded beads were washed with buffer with increasing imidazole concentrations (20 mM NaPi at pH 7.5, 300 mM NaCl, 5% glycerol, 15–30 mM imidazole, 0.5 mM TCEP, 0.03% DDM). The proteins were eluted from the column with a buffer containing high imidazole concentration (20 mM NaPi at pH 7.5, 150 mM NaCl, 5% glycerol, 250 mM imidazole, 0.5 mM TCEP, 0.03% DDM) and combined with 1 mg of TEV protease to perform the His-tag cleavage during dialysis overnight at 4°C . The dialysis buffer contained 20 mM HEPES at pH 7.5, 150 mM NaCl, 5% glycerol, 0.5 mM TCEP, 0.03% DDM. The cleaved protein was recovered by negative IMAC, concentrated to 4 ml using a 50 kDa concentrator (Corning[®] Spin-X[®] UF concentrators) and run on an ÄKTA Pure system (GE Healthcare Life Sciences), using a HiLoad 16/ 600 Superdex 200 column for DtpC, and a Superdex 200 Increase 10/300 column for the split sfGFP-DtpC constructs. Fractions containing the protein were pooled, concentrated, flash frozen and stored at -80°C until further use.

For the split sfGFP-*HsPepT1* constructs, expression was done in mammalian cells as described previously (Pieprzyk et al., 2018; Killer et al., 2021). Briefly, HEK293F cells were collected 48 h after transient transfection, and stored at -80°C until further use. Frozen cell pellets were resuspended in 300 mM NaCl, 20 mM NaPi (pH 7.5), 0.5 mM TCEP, and 5% glycerol, supplemented with cOmplete EDTA-free protease inhibitors, and were disrupted using an Avestin Emulsiflex homogenizer at 10,000–15,000 psi. The lysate was centrifuged for 10 min at $10,000 \times g$, 4°C , and the supernatant was centrifuged for 90 min at $100,000 \times g$, 4°C . The pellet containing the membrane fraction was solubilized in 1% N-Dodecyl- β -D-Maltopyranoside (DDM) and 0.1% cholesteryl hemisuccinate (CHS; Tris Salt, Anatrace) for 1 h at 4°C . The sample was centrifuged for 50 min at $90,000 \times g$, and the supernatant was applied to Strep-TactinXT beads (IBA). After 20 min of incubation on a rotating wheel, the suspension was transferred to a gravity column. Following two wash steps with 300 mM NaCl, 20 mM HEPES (pH 7.5), 0.03% DDM, and 0.003% CHS, split sfGFP-*HsPepT1* constructs were eluted with 0.03% DDM, 0.003% CHS, 150 mM NaCl, 20 mM HEPES (pH 7.5), and 10 mM desthiobiotin (Sigma-Aldrich).

3.2 Selection, Expression and Purification of Nanobodies Against DtpC

To generate DtpC specific nanobodies, two non-inbred llamas were injected six times at weekly intervals with a mixture of 94

different proteins including DtpC purified in the detergent DDM ($50 \mu\text{g}$ of each antigen weekly). After 6 weeks of immunization, two separate phage display libraries were constructed, one from each animal, in the pMESy2 vector, which is a derivative of pMESy4 that contain a C-terminal EPEA-tag for affinity purification. After pooling both libraries, nanobodies were selected against individual antigens in two rounds of parallel panning in 96-well plates containing one immobilized antigen in each well. After two selection rounds on DtpC, 60 clones were picked for sequence analysis, 13 clones encoded antigen-specific nanobodies as tested in ELISA, grouping them in 5 different sequence families. A nanobody family is defined as a group of nanobodies with a high similarity in their CDR3 sequence (identical length and $>80\%$ sequence identity). Nanobodies from the same family derive from the same B-cell lineage and likely bind to the same epitope on the target. Immunizations, library construction, selection by panning and nanobody characterization were performed according to standard procedures (Pardon et al., 2014). Five nanobodies were further characterized.

The nanobodies were expressed in *E. coli* WK6 cells and purified following standard procedures. Specifically, the cell pellet was resuspended in TES buffer (0.2 M TRIS, pH 8, 0.5 mM EDTA, 0.5 M sucrose) supplemented with one protease inhibitor tablet (Roche). Osmotic shock was performed by the addition of diluted TES buffer to release the periplasmic proteins. The solution was first centrifuged for 20 min at $10,000 \times g$ and additionally for 30 min at $100,000 \times g$. The supernatant was applied to CaptureSelect beads (Thermo Fisher Scientific), which were equilibrated with wash buffer (20 mM NaPi, pH 7.5, 20 mM NaCl). After three column volumes of washing, the nanobody was eluted with 20 mM HEPES, pH 7.5, 1.5 M MgCl_2 . The nanobodies were further purified on a HiLoad 16/600 Superdex 75 pg column in 20 mM HEPES, pH 7.5, 150 mM NaCl, 5% glycerol, concentrated with a 5 kDa cut-off concentrator, flash-frozen and stored at -80°C until further use.

3.3 Expression and Purification of Macrobody 26

The nanobody 26 (Nb26) was first inserted into a pBXNPH3 vector containing a C-terminal penta-histidine tag preceded of a HRV-3C protease recognition sequence. The maltose binding protein (MBP) was then inserted in frame with the 3' end of the nanobody, with two proline residues as a linker between the two genes similar as described in (Botte et al., 2021). The resulting Pro-macrobody 26 (Mb26) was expressed in *E. coli* WK6 cells as above. The cell pellet was resuspended in TES buffer (0.2 M TRIS, pH 8, 0.5 mM EDTA, 0.5 M sucrose) supplemented with one protease inhibitor tablet (Roche). Osmotic shock was performed by the addition of diluted TES buffer to release the periplasmic proteins. The solution was first centrifuged for 20 min at $10,000 \times g$ and additionally for 30 min at $142,000 \times g$. The supernatant was further purified by immobilized-metal affinity chromatography (IMAC) on a gravity column. The beads were pre-equilibrated in 20 mM NaPi at pH 7.5, 300 mM NaCl, 5% glycerol, 15–30 mM

imidazole, 0.5 mM TCEP and incubated. Loaded beads were washed with increasing imidazole concentrations (20 mM NaPi at pH 7.5, 300 mM NaCl, 5% glycerol, 15-30 mM imidazole, 0.5 mM TCEP, 0.03% DDM). The proteins were eluted from the column with a buffer containing high imidazole concentration (20 mM NaPi at pH 7.5, 150 mM NaCl, 5% glycerol, 250 mM imidazole, 0.5 mM TCEP, 0.03% DDM) and combined with 1 mg of 3C protease to perform the His-tag cleavage. The cleaved protein was recovered by negative IMAC, concentrated to 0.5 ml using a 30 kDa concentrator (Corning® Spin-X® UF concentrators) and run on an ÄKTA Pure system (GE Healthcare Life Sciences), using a Superdex 75 Increase 10/300 column. Fractions containing the protein were pooled, concentrated, flash frozen and stored at -80°C until further use.

3.4 Thermal Stability Measurements

The differential scanning fluorimetry method was used to follow the thermal unfolding event (Kotov et al., 2019) of Nb17, Nb26, Nb38, DtpC, DtpC-Nb17, DtpC-Nb26, DtpC-Nb38, Mb26, DtpC-Mb26, and split sfGFP-DtpC₁₋₄₇₅-Nb26 with a Prometheus NT.48 device (NanoTemper Technologies, Munich, Germany). The purified proteins were diluted to 16 μM, and the complexes were formed using a 1:1.5 M ratio of membrane protein: fiducial. The fluorescence at 330 and 350 nm was recorded over a temperature gradient scan from 15° to 95°C and processed in GraphPad Prism 9.0 (GraphPad Software).

3.5 AlphaFold2 Predictions

Structures with the following sequences were used as input for AlphaFold2 structure prediction (Jumper et al., 2021), and AMBER relaxation. The best ranked models were used for visualization.

3.5.1 Split sfGFP-DtpC₁₋₄₇₅

MSKGEELFTGVVPILVELDGDVNGHKFSVRGEGEGDATNG
KLTCLKFICTTGKLPVWPPTLVTTLYGVQCFSRYPDHMKR
RHDFKSAPEGYVQERTISFKDDGTYKTRAEVKFECDTLV
NRIELKIDFKEDGNILGHKLEYNKTPSQPRAIYYIVAIQIWE
YFSFYGMRAILLILYLTHQLGFDDNHAIKLSFASLVYVTP
LGGWLADRLGNRTAVIAGALLMTLGHVVLGIDTNSFTSL
YLALAIICGGLFKSNISCLLGEYDENDHRRDGGFSLLYA
AGNIGSIAAPIACGLAAQWYGVHVFALAGGGMFIGLLIF
LSGHRHFQSTRSMDKKALTSVKFALPVWSWLVVMLCLA
PVFFTTLLLENDWSGYLLAIVCLIAAQIARMMIKPFPEHRRAL
WQIVLLMFVGTFLFWVLAQQGGSTISLFDIFRVNRQAFNIEV
PTALFQSVNAIAVMLAGVVLAWLASPESRGNSTLVRWLKFA
FGLLLMACGFMLLAFDARHAAADGQASMGVMISGLAL
MGFAELFIDPVAIAQITRLKMSGVLTGIYMLATGAVANW
LAGVVAQQTTSQISGMAIAAYQRFFSQMGEWTLACVAI
IVVLAFAFTRFLFSTPNSHNVYITADKQKNGIKANFKIRHN
VEDGSVQLADHYQQNTPIGDGPVLLPDNHYLSTQSVLSK
D PNEKRDHMLLEFVTAAGITHGMDELYK.

3.5.2 Split sfGFP-DtpC_{FL}

MSKGEELFTGVVPILVELDGDVNGHKFSVRGEGEGDATN
GKLTCLKFICTTGKLPVWPPTLVTTLYGVQCFSRYPDHMK

RHDFKSAPEGYVQERTISFKDDGTYKTRAEVKFECDTLV
LVNRIELKIDFKEDGNILGHKLEYNKTPSQPRAIYYIVAIQ
IWEYFSFYGMRAILLILYLTHQLGFDDNHAIKLSFASLVY
VTPILGGWLADRLGNRTAVIAGALLMTLGHVVLGIDTNS
TFSLYLALAIICGGLFKSNISCLLGEYDENDHRRDGGFSL
LLYAAGNIGSIAAPIACGLAAQWYGVHVFALAGGGMFIG
LLIFLSGHRHFQSTRSMDKKALTSVKFALPVWSWLVVML
CLAPVFFTTLLLENDWSGYLLAIVCLIAAQIARMMIKPFPEH
RALWQIVLLMFVGTFLFWVLAQQGGSTISLFDIFRVNRQAF
NIEVPTALFQSVNAIAVMLAGVVLAWLASPESRGNSTLVR
WLKFAFGLLLMACGFMLLAFDARHAAADGQASMGVMI
SGLALMGFAELFIDPVAIAQITRLKMSGVLTGIYMLATGAV
ANWLAGVVAQQTTSQISGMAIAAYQRFFSQMGEWTL
ACVAIIVVLAFAFTRFLFSTPNMIQESNDNSHNVYITADKQ
KNGIKANFKIRHNVEDGSVQLADHYQQNTPIGDGPVLLP
DNHYLSTQSVLSKDPNEKRDHMLLEFVTAAGITHGMDE
LYK.

3.5.3 Split sfGFP-DtpC_{+5Gly}

MSKGEELFTGVVPILVELDGDVNGHKFSVRGEGEGDATN
GKLTCLKFICTTGKLPVWPPTLVTTLYGVQCFSRYPDHMK
RHDFKSAPEGYVQERTISFKDDGTYKTRAEVKFECDTLV
LVNRIELKIDFKEDGNILGHKLEYNKTPSQPRAIYYIVAIQI
WEYFSFYGMRAILLILYLTHQLGFDDNHAIKLSFASLVYV
TPILGGWLADRLGNRTAVIAGALLMTLGHVVLGIDTNSFT
FSLYLALAIICGGLFKSNISCLLGEYDENDHRRDGGFSL
YAAGNIGSIAAPIACGLAAQWYGVHVFALAGGGMFIGLL
IFLSGHRHFQSTRSMDKKALTSVKFALPVWSWLVVMLC
LAPVFFTTLLLENDWSGYLLAIVCLIAAQIARMMIKPFPEHRR
ALWQIVLLMFVGTFLFWVLAQQGGSTISLFDIFRVNRQA
FNIEVPTALFQSVNAIAVMLAGVVLAWLASPESRGNSTLVR
WLKFAFGLLLMACGFMLLAFDARHAAADGQASMGVMI
SGLALMGFAELFIDPVAIAQITRLKMSGVLTGIYMLATGAV
ANWLAGVVAQQTTSQISGMAIAAYQRFFSQMGEWTL
ACVAIIVVLAFAFTRFLFSTPNMIQESNDGGGGGNSHNVY
ITADKQKNGIKANFKIRHNVEDGSVQLADHYQQNTPIGDG
PVLLPDNHYLSTQSVLSKDPNEKRDHMLLEFVTAAGITH
GMDELYK.

3.6 Cryo-EM Sample Preparation, Data Collection, Image Analysis, and Atomic Modelling

One hour before vitrification, the purified protein complexes were thawed on ice and run on a Superdex Increase 200 5/150 column in 0.015% DDM, 100 mM NaCl, 10 mM HEPES (pH 7.5), 0.5 mM TCEP in order to remove the excess of empty detergent micelles earlier generated upon sample concentration. The top fraction reached a concentration ranging between 3 and 6 mg/ml, and for each sample, 3.6 μl were applied to glow-discharged gold holey carbon 2/1 300-mesh grids (Quantifoil). Grids were blotted for 4 s at 0 force and 1-s wait time before being vitrified in liquid propane using a Mark IV Vitrobot (Thermo Fisher Scientific). The blotting chamber was maintained at 4°C and 100% humidity during freezing.

All movies were collected using a Titan Krios (Thermo Fisher Scientific) outfitted with a K3 camera and BioQuantum energy

filter (Gatan) set to 10 eV. Automated data acquisitions were set using EPU (Thermo Fisher Scientific). The applied defocus ranged between $-0.9\ \mu\text{m}$ and $-1.8\ \mu\text{m}$ in all datasets.

For DtpC-Nb26 and DtpC-Mb26, movies were collected at a nominal magnification of $\times 105,000$ and a physical pixel size of $0.85\ \text{\AA}$, with a $70\text{-}\mu\text{m}$ C2 aperture and $100\text{-}\mu\text{m}$ objective aperture at a dose rate of $19.5\ \text{e}/\text{pixel}$ per second. A total dose of $75\ \text{e}/\text{\AA}^2$ was used with 2.8 s exposure time, fractionated in 50 frames. For split sfGFP-DtpC₁₋₄₇₅-Nb26, movies were collected at a nominal magnification of $\times 130,000$ and a physical pixel size of $0.67\ \text{\AA}$, with a $50\text{-}\mu\text{m}$ C2 aperture and $100\text{-}\mu\text{m}$ objective aperture at a dose rate of $19.0\ \text{e}/\text{pixel}$ per second. A total dose of $57\ \text{e}/\text{\AA}^2$ was used with 3 s exposure time fractionated in 40 frames.

All movies were motion-corrected using Relion-3.1 (Scheres, 2012; Zivanov et al., 2018) own implementation of MotionCor2 (Zheng et al., 2017). Contrast transfer function parameters were calculated using CTFFIND4 (Rohou and Grigorieff, 2015) and putative particle coordinates were initially defined using CrYOLO (Wagner et al., 2019).

For DtpC-Mb26, 13,257 movies were collected, 3,062,337 coordinates were picked and used for 2D averaging and clustering. For split sfGFP-DtpC₁₋₄₇₅-Nb26, 7602 movies were collected, 1,049,399 coordinates were picked and used for 2D averaging and clustering. For DtpC-Nb26, 24,333 movies were collected, 6,464,070 coordinates were picked and used for 2D averaging and clustering, and 878,428 particles were used in the final 3D reconstruction. Briefly, DtpC-Nb26 dimeric population was clustered using 3D class averaging in Relion3.1 (Scheres, 2012). Particle trajectories and cumulative beam damage were further corrected by Bayesian polishing in Relion3.1 (Zivanov et al., 2019), and the resulting shiny particles were exported to cryoSPARCv3 (Punjani et al., 2017) for further 3D clustering via successive heterogeneous refinement cycles using “bad” and “good” volumes as references to denoise the dataset. Non uniform refinement (Punjani et al., 2020), followed by a local refinement using a soft mask around one transporter unit resulted in a $2.7\ \text{\AA}$ reconstruction of DtpC. The overall resolution was estimated in CryoSPARCv3 using the FSC = 0.143 cutoff. Local resolution estimations were also calculated in CryoSPARCv3 using the 0.5 FSC cutoff. The two half maps were used as inputs to assess various post-processing strategies such as the CryoSPARC’s sharpening tool, DeepEMhancer (Sanchez-Garcia et al., 2021), and Resolve_cryo-em (Terwilliger et al., 2020). The latter led to a slightly better defined contour of the atoms, and was subsequently used for the last atomic-model refinement of DtpC. The initial models of DtpC and Nb26 were generated using AlphaFold2, and refined against the experimental maps; first in Isolde (Croll, 2018), and last in Phenix (Afonine et al., 2018), principally to refine atomic displacement parameters (B-factors) and perform a slight energy minimization while keeping restrains from Isolde’s reference model. Half-maps, and postprocessed maps of the dimeric arrangement and of the focused refinement, as well as the atomic model of DtpC were deposited in the PDB and EMDB as deposition numbers 7ZC2,

and EMD-14618. The atomic model of the dimeric DtpC-Nb26 is available upon request.

3.7 Small-Angle X-Ray Scattering Data Collection and Analysis

Synchrotron SAXS data from solutions of DtpC-Nb26 in β -DDM micelles (SEC-SAXS) were collected on the EMBL P12 (Blanchet et al., 2015) beamline at the PETRA III storage ring (Hamburg, Germany), in a buffer consisting of 0.015% DDM, 100 mM NaCl, 10 mM HEPES (pH 7.5), and 0.5 mM TCEP. Sample (10 mg/ml) was injected onto a Superdex Increase 200 10/300 column (Cytiva) and run at 0.5 ml/min at 20°C . 3000 successive 1 s frames were collected using a Pilatus 2M detector at a sample-detector distance of 3.1 m and at a wavelength of $\lambda = 0.124\ \text{nm}$ ($I(s)$ vs. s , where $s = 4\pi\sin\theta/\lambda$, and 2θ is the scattering angle). The data were normalized to the intensity of the transmitted beam and radially averaged; the scattering of the solvent-blank was subtracted using CHROMIXS (Panjkovich and Svergun, 2018). Cryo-EM volume maps of DtpC-Nb26 were fit to the scattering data across the low-angle range (shape region only) using EM2DAM (Franke et al., 2017) at a density threshold of 0.1.

3.8 Data Visualization

Graphs were generated using GraphPad Prism 9.0 (GraphPad Software). Molecular graphics and analyses performed with UCSF ChimeraX-1.2.5 (Pettersen et al., 2021). Figures were prepared in Adobe Illustrator 2021.

DATA AVAILABILITY STATEMENT

The datasets presented in this study can be found in online repositories. The names of the repository/repositories and accession number(s) can be found below: <http://www.wwpdb.org/>, 7ZC2 <https://www.ebi.ac.uk/pdbe/emdb/>, EMD-14618.

AUTHOR CONTRIBUTIONS

Conceptualization: MK, CL. Methodology: MK, GF, HM, EP. Investigation: MK, GF, HM, EP. Visualization: MK, HM. Funding acquisition: DS, JS, CL. Project administration: CL. Supervision: DS, JS, CL. Writing—original draft: MK, CL. Writing—review and editing: MK, GF, HM, DS, EP, JS, CL.

FUNDING

This work was supported by a grant from the BMBF (grant number: 05K18YEA). Part of this work was performed at the CryoEM Facility at CSSB, supported by the UHH and DFG grant numbers (INST 152/772-1|152/774-1|152/775-1|152/776-1|152/777-1 FUGG).

ACKNOWLEDGMENTS

We thank the Sample Preparation and Characterization facility of EMBL Hamburg for support in this project and the beamlines P13 and P14 at EMBL Hamburg for regular access. We acknowledge Instruct-ERIC and the FWO for their support to the Nb discovery and Saif Saifuzzaman for the technical assistance during Nb discovery. All past and current group members are acknowledged for their input to this

REFERENCES

- Aduri, N. G., Prabhala, B. K., Ernst, H. A., Jørgensen, F. S., Olsen, L., and Mirza, O. (2015). Salt Bridge Swapping in the EXXERFYXX Motif of Proton-Coupled Oligopeptide Transporters. *J. Biol. Chem.* 290, 29931–29940. doi:10.1074/jbc.M115.675603
- Afonine, P. V., Poon, B. K., Read, R. J., Sobolev, O. V., Terwilliger, T. C., Urzhumtsev, A., et al. (2018). Real-space Refinement inPHENIX for Cryo-EM and Crystallography. *Acta Cryst. Sect. D. Struct. Biol.* 74, 531–544. doi:10.1107/S2059798318006551
- Bartels, K., Lasitzka-Male, T., Hofmann, H., and Löw, C. (2021). Single-Molecule FRET of Membrane Transport Proteins. *ChemBiochem* 22, 2657–2671. doi:10.1002/cbic.202100106
- Blanchet, C. E., Spilotos, A., Schwemmer, F., Graewert, M. A., Kikhney, A., Jeffries, C. M., et al. (2015). Versatile Sample Environments and Automation for Biological Solution X-Ray Scattering Experiments at the P12 Beamline (PETRA III, DESY). *J. Appl. Cryst.* 48, 431–443. doi:10.1107/S160057671500254X
- Boggavarapu, R., Jeckelmann, J.-M., Harder, D., Ucurum, Z., and Fotiadis, D. (2015). Role of Electrostatic Interactions for Ligand Recognition and Specificity of Peptide Transporters. *BMC Biol.* 13, 58. doi:10.1186/s12915-015-0167-8
- Botte, M., Ni, D., Schenck, S., Zimmermann, I., Chami, M., Bocquet, N., et al. (2022). Cryo-EM Structures of a LptDE Transporter in Complex with Promacrobodies Offer Insight into Lipopolysaccharide Translocation. *Nat. Commun.* 13, 1826. doi:10.1038/s41467-022-29459-2
- Brandsch, M., Knütter, I., and Leibach, F. H. (2004). The Intestinal H⁺/peptide Symporter PEPT1: Structure-Affinity Relationships. *Eur. J. Pharm. Sci.* 21, 53–60. doi:10.1016/s0928-0987(03)00142-8
- Brandsch, M. (2009). Transport of Drugs by Proton-Coupled Peptide Transporters: Pearls and Pitfalls. *Expert Opin. Drug Metabolism Toxicol.* 5, 887–905. doi:10.1517/17425250903042292
- Brunner, J. D., Jakob, R. P., Schulze, T., Neldner, Y., Moroni, A., Thiel, G., et al. (2020). Structural Basis for Ion Selectivity in TMEM175 K⁺ Channels. *Elife* 9, e53683. doi:10.7554/eLife.53683
- Chen, X.-Z., Steel, A., and Hediger, M. A. (2000). Functional Roles of Histidine and Tyrosine Residues in the H⁺-Peptide Transporter PepT1. *Biochem. Biophysical Res. Commun.* 272, 726–730. doi:10.1006/bbrc.2000.2851
- Colas, C., Masuda, M., Sugio, K., Miyauchi, S., Hu, Y., Smith, D. E., et al. (2017). Chemical Modulation of the Human Oligopeptide Transporter 1, hPepT1. *Mol. Pharm.* 14, 4685–4693. doi:10.1021/acs.molpharmaceut.7b00775
- Croll, T. I. (2018). ISOLDE: a Physically Realistic Environment for Model Building into Low-Resolution Electron-Density Maps. *Acta Cryst. Sect. D. Struct. Biol.* 74, 519–530. doi:10.1107/S2059798318002425
- Daniel, H. (2004). Molecular and Integrative Physiology of Intestinal Peptide Transport. *Annu. Rev. Physiol.* 66, 361–384. doi:10.1146/annurev.physiol.66.032102.144149
- Daniel, H., Spanier, B., Kottra, G., and Weitz, D. (2006). From Bacteria to Man: Archaic Proton-dependent Peptide Transporters at Work. *Physiology* 21, 93–102. doi:10.1152/physiol.00054.2005
- Doki, S., Kato, H. E., Solcan, N., Iwaki, M., Koyama, M., Hattori, M., et al. (2013). Structural Basis for Dynamic Mechanism of Proton-Coupled Symport by the Peptide Transporter POT. *Proc. Natl. Acad. Sci. U.S.A.* 110, 11343–11348. doi:10.1073/pnas.1301079110
- Drew, D., and Boudker, O. (2016). Shared Molecular Mechanisms of Membrane Transporters. *Annu. Rev. Biochem.* 85, 543–572. doi:10.1146/annurev-biochem-060815-014520

manuscript and their efforts to crystallize DtpC over the years.

SUPPLEMENTARY MATERIAL

The Supplementary Material for this article can be found online at: <https://www.frontiersin.org/articles/10.3389/fmolb.2022.917725/full#supplementary-material>

- Drew, D., North, R. A., Nagarathinam, K., and Tanabe, M. (2021). Structures and General Transport Mechanisms by the Major Facilitator Superfamily (MFS). *Chem. Rev.* 121, 5289–5335. doi:10.1021/acs.chemrev.0c00983
- Ernst, H. A., Pham, A., Hald, H., Kastrop, J. S., Rahman, M., and Mirza, O. (2009). Ligand Binding Analyses of the Putative Peptide Transporter YjdL from *E. coli* Display a Significant Selectivity towards Dipeptides. *Biochem. Biophysical Res. Commun.* 389, 112–116. doi:10.1016/j.bbrc.2009.08.098
- Foley, D., Rajamanickam, J., Bailey, P., and Meredith, D. (2010). Bioavailability through PepT1: the Role of Computer Modelling in Intelligent Drug Design. *Curr. Comput. Aided Drug Des.* 6, 68–78. doi:10.2174/157340910790980133
- Franke, D., Petoukhov, M. V., Konarev, P. V., Panjkovich, A., Tuukkanen, A., Mertens, H. D. T., et al. (2017). ATSAS 2.8: a Comprehensive Data Analysis Suite for Small-Angle Scattering from Macromolecular Solutions. *J. Appl. Cryst.* 50, 1212–1225. doi:10.1107/S1600576717007786
- Gabrielsen, M., Kroner, F., Black, L., Isaacs, N. W., Roe, A. J., and McLuskey, K. (2011). High-throughput Identification of Purification Conditions Leads to Preliminary Crystallization Conditions for Three Inner Membrane Proteins. *Mol. Membr. Biol.* 28, 445–453. doi:10.3109/09687688.2011.628954
- Guettou, F., Quistgaard, E. M., Raba, M., Moberg, P., Löw, C., and Nordlund, P. (2014). Selectivity Mechanism of a Bacterial Homolog of the Human Drug-Peptide Transporters PepT1 and PepT2. *Nat. Struct. Mol. Biol.* 21, 728–731. doi:10.1038/nsmb.2860
- Guettou, F., Quistgaard, E. M., Trésaugues, L., Moberg, P., Jegerschöld, C., Zhu, L., et al. (2013). Structural Insights into Substrate Recognition in Proton-dependent Oligopeptide Transporters. *EMBO Rep.* 14, 804–810. doi:10.1038/embor.2013.107
- Harder, D., Stolz, J., Casagrande, F., Obrdlík, P., Weitz, D., Fotiadis, D., et al. (2008). DtpB (YhiP) and DtpA (TppB, YdGR) Are Prototypical Proton-dependent Peptide Transporters of *Escherichia coli*. *FEBS J.* 275, 3290–3298. doi:10.1111/j.1742-4658.2008.06477.x
- Hediger, M. A., Cléménçon, B., Burrier, R. E., and Bruford, E. A. (2013). The ABCs of Membrane Transporters in Health and Disease (SLC Series): Introduction. *Mol. Aspects Med.* 34, 95–107. doi:10.1016/j.mam.2012.12.009
- Heinz, L. X., Lee, J., Kapoor, U., Kartnig, F., Sedlyarov, V., Papakostas, K., et al. (2020). TASL Is the SLC15A4-Associated Adaptor for IRF5 Activation by TLR7-9. *Nature* 581, 316–322. doi:10.1038/s41586-020-2282-0
- Hillgren, K. M., Keppler, D., Zur, A. A., Giacomini, K. M., Stieger, B., Cass, C. E., et al. (2013). Emerging Transporters of Clinical Importance: an Update from the International Transporter Consortium. *Clin. Pharmacol. Ther.* 94, 52–63. doi:10.1038/clpt.2013.74
- Ingersoll, S. A., Ayyadurai, S., Charania, M. A., Laroui, H., Yan, Y., and Merlin, D. (2012). The Role and Pathophysiological Relevance of Membrane Transporter PepT1 in Intestinal Inflammation and Inflammatory Bowel Disease. *Am. J. Physiology-Gastrointestinal Liver Physiology* 302, G484–G492. doi:10.1152/ajpgi.00477.2011
- Jardetzky, O. (1966). Simple Allosteric Model for Membrane Pumps. *Nature* 211, 969–970. doi:10.1038/211969a0
- Jensen, J. M., Aduri, N. G., Prabhala, B. K., Jahnsen, R., Franzyk, H., and Mirza, O. (2014). Critical Role of a Conserved Transmembrane Lysine in Substrate Recognition by the Proton-Coupled Oligopeptide Transporter YjdL. *Int. J. Biochem. Cell Biol.* 55, 311–317. doi:10.1016/j.biocel.2014.09.016
- Jensen, J. M., Ernst, H., Wang, X., Hald, H., Ditta, A. C., Ismat, F., et al. (2012a). Functional Investigation of Conserved Membrane-Embedded Glutamate Residues in the Proton-Coupled Peptide Transporter YjdL. *Protein Pept. Lett.* 19, 282–287. doi:10.2174/092986612799363109

- Jensen, J. M., Ismat, F., Szakonyi, G., Rahman, M., and Mirza, O. (2012b). Probing the Putative Active Site of YjdL: an Unusual Proton-Coupled Oligopeptide Transporter from *E. coli*. *PLoS One* 7, e47780. doi:10.1371/journal.pone.0047780
- Jensen, J. M., Simonsen, F. C., Mastali, A., Hald, H., Lillebro, I., Diness, F., et al. (2012c). Biophysical Characterization of the Proton-Coupled Oligopeptide Transporter YjdL. *Peptides* 38, 89–93. doi:10.1016/j.peptides.2012.08.012
- Jumper, J., Evans, R., Pritzel, A., Green, T., Figurnov, M., Ronneberger, O., et al. (2021). Highly Accurate Protein Structure Prediction with AlphaFold. *Nature* 596, 583–589. doi:10.1038/s41586-021-03819-2
- Killer, M., Wald, J., Pieprzyk, J., Marlovits, T. C., and Löw, C. (2021). Structural Snapshots of Human PepT1 and PepT2 Reveal Mechanistic Insights into Substrate and Drug Transport across Epithelial Membranes. *Sci. Adv.* 7, eabk3259. doi:10.1126/sciadv.abk3259
- Kotov, V., Bartels, K., Veith, K., Josts, I., Subhramanyam, U. K. T., Günther, C., et al. (2019). High-throughput Stability Screening for Detergent-Solubilized Membrane Proteins. *Sci. Rep.* 9, 10379. doi:10.1038/s41598-019-46686-8
- Liu, S., Li, S., Krezel, A. M., and Li, W. (2022). Stabilization and Structure Determination of Integral Membrane Proteins by Termini Restraining. *Nat. Protoc.* 17, 540–565. doi:10.1038/s41596-021-00656-5
- Liu, S., Li, S., Yang, Y., and Li, W. (2020). Termini Restraining of Small Membrane Proteins Enables Structure Determination at Near-Atomic Resolution. *Sci. Adv.* 6, eabe3717. doi:10.1126/sciadv.abe3717
- Löw, C., Jegerschöld, C., Kovermann, M., Moberg, P., and Nordlund, P. (2012). Optimisation of Over-expression in *E. coli* and Biophysical Characterisation of Human Membrane Protein Synaptogyrin 1. *PLoS One* 7, e38244. doi:10.1371/journal.pone.0038244
- Löw, C., Moberg, P., Quistgaard, E. M., Hedrén, M., Guettou, F., Frauenfeld, J., et al. (2013). High-throughput Analytical Gel Filtration Screening of Integral Membrane Proteins for Structural Studies. *Biochimica Biophysica Acta (BBA) - General Subj.* 1830, 3497–3508. doi:10.1016/j.bbagen.2013.02.001
- Lyons, J. A., Parker, J. L., Solcan, N., Brinth, A., Li, D., Shah, S. T., et al. (2014). Structural Basis for Polyspecificity in the POT Family of Proton-coupled Oligopeptide Transporters. *EMBO Rep.* 15, 886–893. doi:10.15252/embr.201338403
- Martinez Molledo, M., Quistgaard, E. M., Flayhan, A., Pieprzyk, J., and Löw, C. (2018a). Multispecific Substrate Recognition in a Proton-dependent Oligopeptide Transporter. *Structure* 26, 467–476. e4. doi:10.1016/j.str.2018.01.005
- Martinez Molledo, M., Quistgaard, E. M., and Löw, C. (2018b). Tripeptide Binding in a Proton-dependent Oligopeptide Transporter. *FEBS Lett.* 592, 3239–3247. doi:10.1002/1873-3468.13246
- Minhas, G. S., Bawdon, D., Herman, R., Rudden, M., Stone, A. P., James, A. G., et al. (2018). Structural Basis of Malodour Precursor Transport in the Human Axilla. *Elife* 7, e34995. doi:10.7554/eLife.34995
- Nagamura, R., Fukuda, M., Kawamoto, A., Matoba, K., Dohmae, N., Ishitani, R., et al. (2019). Structural Basis for Oligomerization of the Prokaryotic Peptide Transporter PepTSo2. *Acta Cryst. Sect. F* 75, 348–358. doi:10.1107/S2053230X19003546
- Newstead, S., Drew, D., Cameron, A. D., Postis, V. L. G., Xia, X., Fowler, P. W., et al. (2011). Crystal Structure of a Prokaryotic Homologue of the Mammalian Oligopeptide-Proton Symporters, PepT1 and PepT2. *EMBO J.* 30, 417–426. doi:10.1038/emboj.2010.309
- Panjikovich, A., and Svergun, D. I. (2018). CHROMIXS: Automatic and Interactive Analysis of Chromatography-Coupled Small-Angle X-Ray Scattering Data. *Bioinformatics* 34, 1944–1946. doi:10.1093/bioinformatics/btx846
- Pardon, E., Laeremans, T., Triest, S., Rasmussen, S. G. F., Wohlkönig, A., Ruf, A., et al. (2014). A General Protocol for the Generation of Nanobodies for Structural Biology. *Nat. Protoc.* 9, 674–693. doi:10.1038/nprot.2014.039
- Parker, J. L., Deme, J. C., Wu, Z., Kuteyi, G., Huo, J., Owens, R. J., et al. (2021). Cryo-EM Structure of PepT2 Reveals Structural Basis for Proton-Coupled Peptide and Prodrug Transport in Mammals. *Sci. Adv.* 7, eabh3355. doi:10.1126/sciadv.abh3355
- Pettersen, E. F., Goddard, T. D., Huang, C. C., Meng, E. C., Couch, G. S., Croll, T. I., et al. (2021). UCSF ChimeraX : Structure Visualization for Researchers, Educators, and Developers. *Protein Sci.* 30, 70–82. doi:10.1002/pro.3943
- Pieprzyk, J., Pazicky, S., and Löw, C. (2018). Transient Expression of Recombinant Membrane-eGFP Fusion Proteins in HEK293 Cells. *Methods Mol. Biol.* 1850, 17–31. doi:10.1007/978-1-4939-8730-6_2
- Prabhala, B. K., Aduri, N. G., Iqbal, M., Rahman, M., Gajhede, M., Hansen, P. R., et al. (2017). Several hPepT1-Transported Drugs Are Substrates of the *Escherichia coli* Proton-Coupled Oligopeptide Transporter YdgR. *Res. Microbiol.* 168, 443–449. doi:10.1016/j.resmic.2017.01.005
- Prabhala, B. K., Aduri, N. G., Jensen, J. M., Ernst, H. A., Iram, N., Rahman, M., et al. (2014). New Insights into the Substrate Specificities of Proton-Coupled Oligopeptide Transporters from *E. coli* by a pH Sensitive Assay. *FEBS Lett.* 588, 560–565. doi:10.1016/j.febslet.2014.01.004
- Prabhala, B. K., Aduri, N. G., Sharma, N., Shaheen, A., Sharma, A., Iqbal, M., et al. (2018). The Prototypical Proton-Coupled Oligopeptide Transporter YdgR from *Escherichia coli* Facilitates Chloramphenicol Uptake into Bacterial Cells. *J. Biol. Chem.* 293, 1007–1017. doi:10.1074/jbc.M117.805960
- Punjani, A., and Fleet, D. J. (2021). 3D Variability Analysis: Resolving Continuous Flexibility and Discrete Heterogeneity from Single Particle Cryo-EM. *J. Struct. Biol.* 213, 107702. doi:10.1016/j.jsb.2021.107702
- Punjani, A., Rubinstein, J. L., Fleet, D. J., and Brubaker, M. A. (2017). cryoSPARC: Algorithms for Rapid Unsupervised Cryo-EM Structure Determination. *Nat. Methods* 14, 290–296. doi:10.1038/nmeth.4169
- Punjani, A., Zhang, H., and Fleet, D. J. (2020). Non-uniform Refinement: Adaptive Regularization Improves Single-Particle Cryo-EM Reconstruction. *Nat. Methods* 17, 1214–1221. doi:10.1038/s41592-020-00990-8
- Quistgaard, E. M., Löw, C., Guettou, F., and Nordlund, P. (2016). Understanding Transport by the Major Facilitator Superfamily (MFS): Structures Pave the Way. *Nat. Rev. Mol. Cell Biol.* 17, 123–132. doi:10.1038/nrm.2015.25
- Quistgaard, E. M., Martinez Molledo, M., and Löw, C. (2017). Structure Determination of a Major Facilitator Peptide Transporter: Inward Facing PepTSt from *Streptococcus Thermophilus* Crystallized in Space Group P3121. *PLoS One* 12, e0173126. doi:10.1371/journal.pone.0173126
- Rohou, A., and Grigorieff, N. (2015). CTFFIND4: Fast and Accurate Defocus Estimation from Electron Micrographs. *J. Struct. Biol.* 192, 216–221. doi:10.1016/j.jsb.2015.08.008
- Sanchez-Garcia, R., Gomez-Blanco, J., Cuervo, A., Carazo, J., Sorzano, C., and Vargas, J. (2021). DeepEMhancer: a Deep Learning Solution for Cryo-EM Volume Post-processing. *Communications Biology*. doi:10.1038/s42003-021-02399-1
- Scheres, S. H. W. (2012). RELION: Implementation of a Bayesian Approach to Cryo-EM Structure Determination. *J. Struct. Biol.* 180, 519–530. doi:10.1016/j.jsb.2012.09.006
- Sharma, N., Aduri, N. G., Iqbal, A., Prabhala, B. K., and Mirza, O. (2016). Peptide Selectivity of the Proton-Coupled Oligopeptide Transporter from *Neisseria Meningitidis*. *J. Mol. Microbiol. Biotechnol.* 26, 312–319. doi:10.1159/000447129
- Shen, J., Hu, M., Fan, X., Ren, Z., Portioli, C., Yan, X., et al. (2022). Extracellular Domain of PepT1 Interacts with TM1 to Facilitate Substrate Transport. *Structure*. S0969-2126(22)00138-1. doi:10.1016/j.str.2022.04.011
- Smith, D. E., Cléménçon, B., and Hediger, M. A. (2013). Proton-coupled Oligopeptide Transporter Family SLC15: Physiological, Pharmacological and Pathological Implications. *Mol. Aspects Med.* 34, 323–336. doi:10.1016/j.mam.2012.11.003
- Solcan, N., Kwok, J., Fowler, P. W., Cameron, A. D., Drew, D., Iwata, S., et al. (2012). Alternating Access Mechanism in the POT Family of Oligopeptide Transporters. *EMBO J.* 31, 3411–3421. doi:10.1038/emboj.2012.157
- Spanier, B., and Rohm, F. (2018). Proton Coupled Oligopeptide Transporter 1 (PepT1) Function, Regulation, and Influence on the Intestinal Homeostasis. *Compr. Physiol.* 8, 843–869. doi:10.1002/cphy.c170038
- Stauffer, M., Jeckelmann, J.-M., Ilgü, H., Ucurum, Z., Boggavarapu, R., and Fotiadis, D. (2022). Peptide Transporter Structure Reveals Binding and Action Mechanism of a Potent PEPT1 and PEPT2 Inhibitor. *Commun. Chem.* 5, 23. doi:10.1038/s42004-022-00636-0
- Terwilliger, T. C., Ludtke, S. J., Read, R. J., Adams, P. D., and Afonine, P. V. (2020). Improvement of Cryo-EM Maps by Density Modification. *Nat. Methods* 17, 923–927. doi:10.1038/s41592-020-0914-9
- Thwaites, D. T., and Anderson, C. M. H. (2007). H⁺-coupled Nutrient, Micronutrient and Drug Transporters in the Mammalian Small Intestine. *Exp. Physiol.* 92, 603–619. doi:10.1113/expphysiol.2005.029959
- Ural-Blimke, Y., Flayhan, A., Strauss, J., Rantos, V., Bartels, K., Nielsen, R., et al. (2019). Structure of Prototypic Peptide Transporter DtpA from *E. coli* in

- Complex with Valganciclovir Provides Insights into Drug Binding of Human PepT1. *J. Am. Chem. Soc.* 141, 2404–2412. doi:10.1021/jacs.8b11343
- Viennois, E., Pujada, A., Zen, J., and Merlin, D. (2018). Function, Regulation, and Pathophysiological Relevance of the POT Superfamily, Specifically PepT1 in Inflammatory Bowel Disease. *Compr. Physiol.* 8, 731–760. doi:10.1002/cphy.c170032
- Wagner, T., Merino, F., Stabrin, M., Moriya, T., Antoni, C., Apelbaum, A., et al. (2019). SPHIRE-crYOLO Is a Fast and Accurate Fully Automated Particle Picker for Cryo-EM. *Commun. Biol.* 2, 218. doi:10.1038/s42003-019-0437-z
- Yan, N. (2015). Structural Biology of the Major Facilitator Superfamily Transporters. *Annu. Rev. Biophys.* 44, 257–283. doi:10.1146/annurev-biophys-060414-033901
- Zhang, Y., Zhang, Y., Sun, K., Meng, Z., and Chen, L. (2019). The SLC Transporter in Nutrient and Metabolic Sensing, Regulation, and Drug Development. *J. Mol. Cell Biol.* 11, 1–13. doi:10.1093/jmcb/mjy052
- Zhao, Y., Mao, G., Liu, M., Zhang, L., Wang, X., and Zhang, X. C. (2014). Crystal Structure of the *E. coli* Peptide Transporter YbgH. *Structure* 22, 1152–1160. doi:10.1016/j.str.2014.06.008
- Zheng, S. Q., Palovcak, E., Armache, J.-P., Verba, K. A., Cheng, Y., and Agard, D. A. (2017). MotionCor2: Anisotropic Correction of Beam-Induced Motion for Improved Cryo-Electron Microscopy. *Nat. Methods* 14, 331–332. doi:10.1038/nmeth.4193
- Zivanov, J., Nakane, T., Forsberg, B. O., Kimanius, D., Hagen, W. J., Lindahl, E., et al. (2018). New Tools for Automated High-Resolution Cryo-EM Structure Determination in RELION-3. *eLife* 7, e42166. doi:10.7554/eLife.42166
- Zivanov, J., Nakane, T., and Scheres, S. H. W. (2019). A Bayesian Approach to Beam-Induced Motion Correction in Cryo-EM Single-Particle Analysis. *Int. Union Crystallogr. J.* 6, 5–17. doi:10.1107/S205225251801463X
- Conflict of Interest:** The authors declare that the research was conducted in the absence of any commercial or financial relationships that could be construed as a potential conflict of interest.
- Publisher's Note:** All claims expressed in this article are solely those of the authors and do not necessarily represent those of their affiliated organizations, or those of the publisher, the editors and the reviewers. Any product that may be evaluated in this article, or claim that may be made by its manufacturer, is not guaranteed or endorsed by the publisher.
- Copyright © 2022 Killer, Finocchio, Mertens, Svergun, Pardon, Steyaert and Löw. This is an open-access article distributed under the terms of the Creative Commons Attribution License (CC BY). The use, distribution or reproduction in other forums is permitted, provided the original author(s) and the copyright owner(s) are credited and that the original publication in this journal is cited, in accordance with accepted academic practice. No use, distribution or reproduction is permitted which does not comply with these terms.